Towards large-scale and spatiotemporally resolved diagnosis of electronic density of states by deep learning

Qiyu Zeng,[1] Bo Chen,[1] Xiaoxiang Yu,[1] Shen Zhang,[1] Dongdong Kang,[1] Han Wang,[2,*] and Jiayu Dai ![ORCID][1,†]

[1]*Department of Physics, National University of Defense Technology, Changsha, Hunan 410073, People's Republic of China*
[2]*Laboratory of Computational Physics, Institute of Applied Physics and Computational Mathematics,*
Beijing 100088, People's Republic of China

Modern laboratory techniques such as ultrafast laser excitation and shock compression can bring matter into highly nonequilibrium states with complex structural transformation, metallization, and dissociation dynamics. To understand and model the dramatic change of both electronic structures and ion dynamics during such dynamic processes, the traditional method faces difficulties. Here, we demonstrate the ability of a deep neural network (DNN) to capture the atomic local-environment dependence of the electronic density of states (DOS) for both multicomponent systems under exoplanet thermodynamic conditions and nonequilibrium systems during superheated melting processes. Large-scale and time-resolved diagnosis of DOS can be efficiently achieved within the accuracy of the *ab initio* method. Moreover, the atomic contribution to DOS given by the DNN model accurately reveals the information of the local neighborhood for the selected atom, which thus can serve as robust order parameters to identify different phases and intermediate local structures, strongly highlighting the efficacy of this DNN model in studying dynamic processes.

I. INTRODUCTION

Modern laboratory techniques such as ultrafast laser excitation and dynamic compression can bring matter into highly nonequilibrium states with complex structural transformation, metallization, and dissociation dynamics [1–4]. By increasing temperatures and pressures in a really short timescale ($\sim 10^{-12}$ s), the behavior of both electrons and ions presents time-dependent characteristics. Especially for the time-resolved diagnosis of electronic structures, it strongly suffers from the complication of a phase transition associated with dramatic changes of the thermodynamic state. The demanding requirements for an accurate description of the electronic structure during dynamic processes raise challenges for all existing methods, and are of great importance for different communities such as condensed matter physics, laboratory astrophysics, planetary physics, material science, and industrial applications [3,5,6].

The classical molecular dynamics simulation (CMD), by integrating Newton's equations of motion for the many-body system, inherently describes the mass transport, energy transport, and phase transition dynamics of ions with a large enough simulation size. However, the lack of an explicit treatment of electrons prevents such a method from describing the evolution of the electronic structure at the same time, while for the *ab initio* method based on quantum mechanics such as density functional theory (DFT), it is too computationally expensive to give the electronic response associated with long-time phase transition dynamics (10^0–10^3 ps) and a large

enough system ($>10^3$ atoms) that involves the coexistence of different phases, gradients of temperatures, and densities.

In past decades, there has been an explosion of attempts to exploit the machine-learning (ML) method to address challenges in the domain of molecular modeling. By directly approximating the solutions of the Kohn-Sham (KS) differential equations, ML models can efficiently yield interatomic potential energy surfaces [7,8] or electronic properties [9–12] with high fidelity. Most recently, ongoing efforts have demonstrated the usefulness of the ML method on the electronic density [9], electronic density of states (DOS) [10,11], and the local density of states (LDOS) [12]. Especially for the DOS, it serves as an important quantity for the identification of the metallization transition and it is intimately related to properties such as electronic heat capacity, electron-phonon coupling, and optical/x-ray absorption spectra [13–16]. Since the existing attempts have been restricted to pure materials under ambient conditions, the ability of the ML model to study a multicomponent system, the temporal and spatial evolution of electronic properties during dynamic processes, has not been validated yet.

Here, we utilize the deep neural network (DNN) to capture the atomic local-environment dependence of DOS, named the DeepDOS model. The accuracy and robustness of the DNN model is verified with a magnesium oxide (MgO) system along an isotherm of 5000 K, with pressures ranging from 236 to 598 GPa. Trained with small-system data sets, the DNN model is able to reproduce the DOS curves with high fidelity for the unseen configurations generated by thermal fluctuations and density variations. Further, this size-extensive model is applied to efficiently study the temporal evolution of DOS curves during dynamics processes within the accuracy of the *ab initio* method. The isobaric melting process of silicon

*wang_han@iapcm.ac.cn
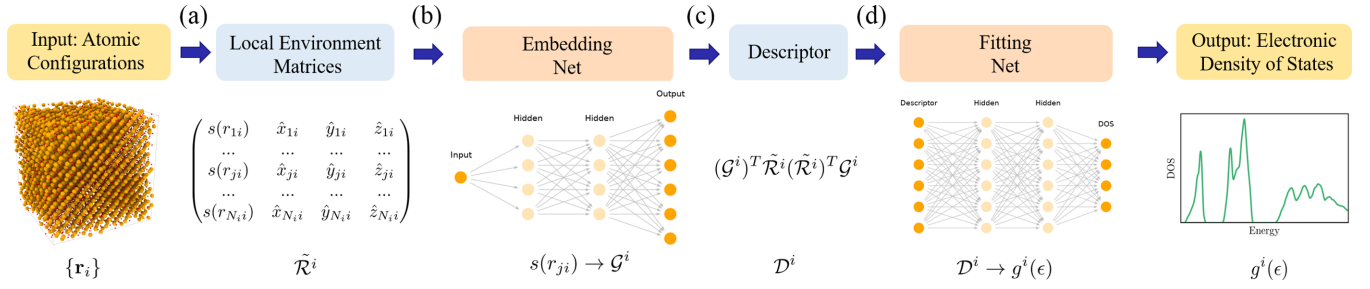†jydai@nudt.edu.cn

174109-1

FIG. 1. Workflow of DeepDOS scheme. (a) Generating the local-environmental matrices $\tilde{\mathcal{R}}^i$ from atomic configurations $\{\mathbf{r}_i\}$ to preserve the translation invariance. (b) Mapping smoothed relative distances $s(r_{ji})$ into M-dimension feature space to obtain local embedding matrices $\mathcal{G}^i$ via an embedding net, where $s(\ldots)$ is the smooth function [17]. (c) Generating descriptor $\mathcal{D}^i$ by multiplication of local embedding matrices and local-environmental matrices to preserve the permutation and rotation invariance. (d) Mapping the descriptor of atom i into the atomic DOS $g^i(\epsilon)$ via a fitting net.

crystalline at a pressure of 5 GPa is chosen. With a large enough system, the coexistence of a solid and liquid phase can be incorporated and the corresponding DOS is given. Moreover, the atomic contribution to DOS accurately reveals the local structure for any selected atoms in this nonequilibrium system, and the DNN-predicted site-projected DOS can be used as a fingerprint to characterize different local structures. This DeepDOS approach provides an efficient tool to study both the electronic structure and ionic local structure during dynamic processes created by shock impact, ultrafast laser heating, etc.

II. METHOD

The machine-learning scheme for DOS prediction is based on two key approximations [10]: (1) The DOS for a configuration can be decomposed into "atomic contributions" so as to preserve the extensive property. (2) Each "atomic contribution" depends on the local environment of the atom, specifically, the relative coordinates of its neighbors within a predefined cutoff radius r_{cut}. The DNN-DOS model can be defined as

$$g(\epsilon) = \sum_i \mathcal{N}_{\alpha_i}[\mathcal{D}_{\alpha_i}(r_i, \{r_j\}_{j \in n(i)})], \qquad (1)$$

where $\mathcal{N}_{\alpha_i}$ denotes the neural network for specified chemical species α_i of atom i, and the descriptor $\mathcal{D}_{\alpha_i}$ describes the local environment of atom i with its neighbor list $n(i) = \{j | r_{ji} < r_{\mathrm{cut}}\}$. Here, we adopted the symmetry-preserving scheme introduced by the deep potential–smooth edition (DeepPot-SE) model [8,17,18] to generate the descriptor.

As illustrated in Fig. 1, the subnetwork consists of an embedding and a fitting neural network. The embedding network is specially designed to map the local environment $\tilde{\mathcal{R}}^i$ to an embedded feature space, which preserves the translational, rotational, and permutational symmetries of the system. The fitting network is a fairly standard fully connected feedforward neural network, which maps the descriptor to the atomic contribution to total DOS, denoted as atomic DOS (ADOS).

To determine the local electronic characteristics, the atomic contribution to DOS serves a key role. In the traditional method, the total DOS is usually used to minimize the loss

function, and is decomposed into ADOS automatically by the machine-learning model [10,11]. Although the total DOS can be well reproduced, the predicted atomic contribution may be inaccurate because only the sum of ADOS is constrained [19]. Here, to accurately describe the different atomic contributions originating from different element types and atomic local environments, the site-projected DOS (PDOS) is used to minimize the loss function. Thus a loss function different from previous works is adopted to optimize the full parameters $\mathbf{w}$ of the DNN, defined as the root-mean-square error (RMSE) of ADOS between the model prediction $g^i_{\mathrm{pred},\mathbf{w}}$ and data set $g^i(\epsilon)$,

$$\mathcal{L}(\mathbf{w}) = \sqrt{\frac{1}{N} \sum_i^N \int_\epsilon \left[g^i_{\mathrm{pred},\mathbf{w}}(\epsilon) - g^i(\epsilon)\right]^2 d\epsilon}. \qquad (2)$$

III. DATA SET

To generate the data set, we perform the deep potential MD (DPMD) simulations to generate trajectories for two different systems with the LAMMPS package [20], and label the configurations along the trajectories: (1) magnesium oxide (MgO, B1 phase) under exoplanet conditions at a temperature of 5000 K, with pressures ranging from 236 to 598 GPa; and (2) heat-until-melt simulations for silicon (cubic diamond phase) under isobaric conditions at a pressure of 5 GPa.

The DP models used in the DPMD simulations for MgO and Si are generated with DeePMD kit packages [18]. To cover a wide range of thermodynamics conditions and minimize the computational consumption, a concurrent learning scheme, deep potential generator (DP-GEN) [21], has been adopted to sample the most compact and adequate data set that guarantees the uniform accuracy of DP in the explored configuration space. More details can be found in the Supplemental Material (SM) [19]. In DPMD simulations, 40-ps-long molecular dynamics trajectories are generated with a time step of 1.0 fs, and the snapshots are collected with an interval of 0.2 ps. To obtain the corresponding site-projected DOS along the trajectories, the QUANTUM ESPRESSO package [22] is used. The Perdew-Burke-Erzerhof (PBE) exchange correlation functional is used [23], and the pseudopotential takes the projector augmented-wave (PAW) formalism [24,25]. The
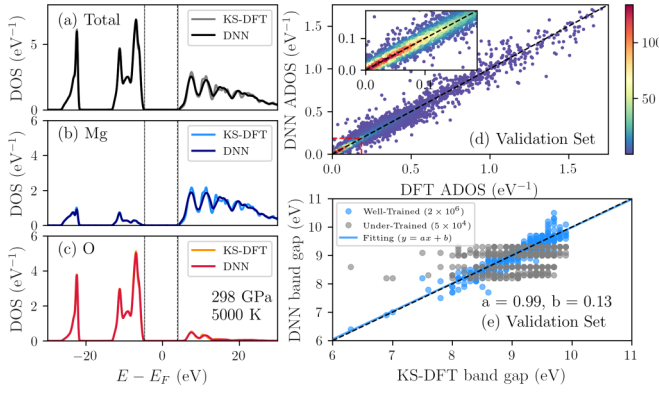
FIG. 2. (a)–(c) Comparison of DOS/ADOS between the KS-DFT calculation and DNN prediction at $p = 298$ GPa, $T = 5000$ K. (d), (e) Parity plot of ADOS/width of the band gap between DFT and DNN prediction in the validation set, where five thermodynamic conditions are included. In (d), the marker color indicates the frequency. In (e), the blue and gray dots represent the predictions of the band gap by the well-trained DNN model (training steps of 2×10^6) and undertrained DNN model (5×10^4), respectively.
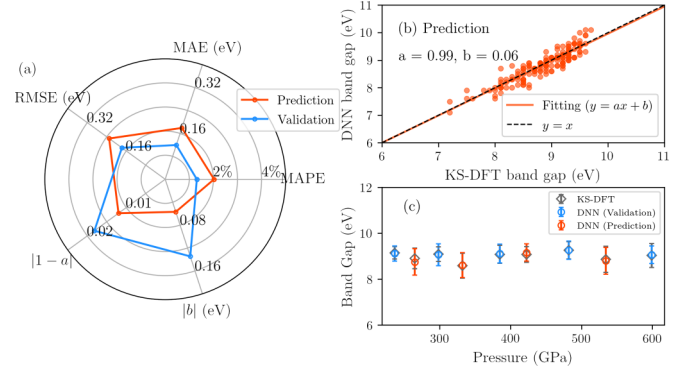

FIG. 3. (a) Radar plot of the test statistics chosen to measure the band gap prediction accuracy for the validation set and test set. (b) DNN-predicted band gaps vs KS-DFT band gaps on the test set. The black dashed line is for visual reference, showing what the exact band gap prediction corresponds to. (c) Configuration-averaged band gaps at different pressures along the isotherm of 5000 K, KS-DFT calculations (gray), and DNN predictions on the validation set (blue) and on the test set (red) are presented.

sampling of the Brillouin zone is chosen as 0.125 Å^{-1}. In the calculation of DOS, Gaussian smearing is used and the width is chosen as 0.02 Ry for MgO and 0.01 Ry for silicon. To train a DeepDOS model, the embedding network is composed of three layers (25, 50, and 100 nodes) while the fitting network has three hidden layers with 240 nodes in each layer. The radius cutoff r_c is chosen to be 6.0 Å.

IV. CAPTURING THERMAL FLUCTUATION AND DENSITY VARIATION

For a finite-temperature system, the ionic thermal motion plays an important role that drives thermal fluctuations both in the atomic local environment and electronic structure. Along the isotherm of the MgO system at 5000 K, ionic thermal motion can introduce significant fluctuations in the $3p$ band of Mg atoms, $2s$ and $2p$ bands of oxygen atoms, indicating that both Mg-ADOS and O-ADOS are sensitive to the atomic local environment even at exoplanet pressures (see Figs. S2 and S3 in SM). The standard deviation of ADOS is $\sigma_1 = 0.136$ eV^{-1} and $\sigma_2 = 0.262$ eV^{-1} for the Mg atom and O atom, respectively. Such a finite-temperature effect can also lead to a large deviation in determining the width of the band gap, varying from ∼6 to ∼9 eV.

Here, we first test the performance of the DNN model on the DOS prediction for this multicomponent system with thermal fluctuated atomic configurations as the input. To train our DNN model, we used a data set covering five different exoplanet pressures from 237 to 599 GPa, with each case containing 400 magnesium site-projected DOS and 400 oxygen site-projected DOS. This data set is randomly divided into a training set and validation set by a ratio of 4 : 1. As presented in Figs. 2(a)–2(c), a well-trained DNN model can accurately reproduce the KS-DFT results of both the total DOS and site-projected DOS for an unseen atomic configuration. Figure 2(d) highlights the consistency between the DNN model and *ab initio* method in predicting the atomic contri-

bution to the number of electronic states $g^i(\epsilon)$ at a specific energy interval $\epsilon + d\epsilon$. The RMSEs of the Mg-ADOS and O-ADOS predictions are $0.115\sigma_1$ and $0.059\sigma_2$, respectively, significantly lower than the standard deviation of the data set.

Moreover, the width of the band gap is extracted from the predicted DOS curve, defined as the interval between the valence band maximum (VBM) and conduction band minimum (CBM). As presented in Fig. 2(e), the alignment of the band gap predictions along the diagonal exhibits small standard deviations for thermally fluctuating atomic configurations. The RMSE on the validation set is 0.17 eV, the mean absolute error (MAE) is 0.11 eV, and the mean absolute percentage error (MAPE) is 1.3%. The model performance on the validation set indicates that the DeepDOS model has the ability to capture the changes of the atomic contribution to the electronic structure induced by thermal fluctuation of the local environment, not only the shape of the DOS curve, but also the detailed structure such as the position of VBM and CBM.

For comparison, the prediction given by an undertrained model (trained with 5×10^4 steps) is presented in Fig. 2(e). Interestingly, for a given thermodynamic condition, the undertrained model failed to describe the subtle difference in electronic states between the thermally fluctuating atomic configurations, leading to several discrete band gap predictions such as a classification model for different thermodynamic conditions.

Further, the variation of density is considered. Since the inhomogeneous density distribution and temperature distribution can be created during dynamic processes, the ability for DNN to predict the unseen configurations for different densities not included in the training set should be checked.

Four interpolated density points within the pressure range of the training data are chosen to generate the data set, denoted as the test set. As presented in Fig. 3(a), the performances of the DeepDOS model in both the validation set and test set show a similar accuracy. In the test set, the RMSE of the band gap prediction is 0.23 eV, the MAE is
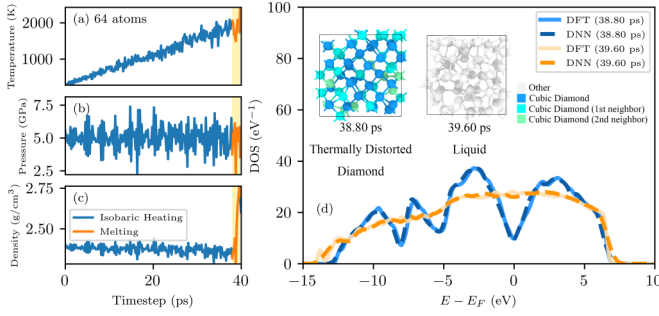
FIG. 4. (a)–(c) Temporal evolution of temperature, pressure, and density during isobaric heating of cubic diamond silicon at 5 GPa (containing 64 atoms), with the orange line indicating the onset of melting. (d) Electronic density of states prediction for the unseen snapshots during the isobaric melting process, where the solid (dashed) line indicates the result from the KS-DFT calculation (DNN prediction). The inset shows the snapshots of the atomic configurations colored by the ext-CNA method [26].
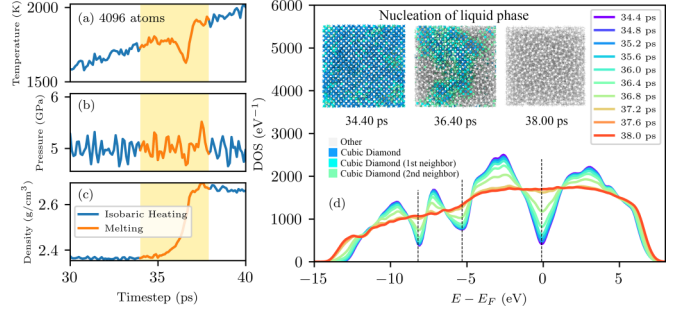

FIG. 5. (a)–(c) Temporal evolution of temperature, pressure, and density during isobaric heating of cubic diamond silicon at 5 GPa (containing 4096 atoms). (d) DOS prediction for the unseen snapshots of the solid-liquid coexistence phase during the process of nucleation and growth of the liquid phase. The black dotted lines mark the three local minima to give the characteristic parameter Q.

0.18 eV, and the MAPE is 2.0%. The DNN-predicted band gaps in Fig. 3(b) are centered around the correct values, thus providing a low bias estimation. The predicted band gaps versus the calculated values from KS-DFT can be fitted to a linear function $y = ax + b$ with a slope $a = 0.99$ and bias $b = 0.06$ eV. The configuration-averaged band gaps at different pressures are presented in Fig. 3(c), where the DNN exhibits a good generalization performance along the isotherm with a pressure-sampling interval of 50 GPa, thus providing a robust prediction in the study of dynamic processes.

V. LARGE-SCALE AND TIME-RESOLVED DOS PREDICTION

By combining nonequilibrium molecular dynamics with the DeepDOS model, we investigate the temporal evolution of DOS during the superheated melting process of silicon, which contains a solid-liquid coexistence, density gradients, and a thermally fluctuating local structure.

The data set containing 1600 silicon site-projected DOS is prepared. The atomic configurations are collected from the heat-until-melt simulation under an isobaric condition, where the cold lattice, and thermally distorted crystalline and liquid phases are included. Different system sizes are considered, and we chose 40 atomic configurations for the 8-atom system, 20 configurations for the 16-atom system, and 10 configurations for the 32-atom system. Moreover, 80 snapshots for the 8-atom system equilibrated at $T = 2000$ K, $p = 5$ GPa are used to improve the description of the disordered structure.

We validate our DeepDOS model by studying the melting process performed with the 64-atom system, where the KS-DFT calculation is affordable. We use DPMD to generate the trajectories for the 64-atom system, and label the configurations along the trajectories by KS-DFT to provide the test set. As shown in Figs. 4(a)–4(c), by heating a silicon system from 300 to 2000 K at 5 GPa, the cubic diamond structure is maintained until 38.80 ps. As the temperature exceeds the limit of thermal stability, the crystal collapses into a disordered structure immediately accompanied by a dramatic change of volume. Correspondingly, the abrupt changes

of the DOS curve induced by the solid-liquid transition can be observed from Fig. 4(d), where DNN predictions show good agreement with KS-DFT calculations for these unseen snapshots of the 64-atom system. Trained with small-system data sets, the DNN model is size extensive to reproduce the DOS curves with a high fidelity for large systems.

Although superheated melting is known to be proceeded by nucleation and growth of liquid regions inside the crystal, due to the limited simulation size, tens or several hundred atoms are not enough to form the liquid cluster according to classic nucleation theory [27,28]. For the removal of such a size effect, simulations are performed with a 4096-atom system, and the DOS evolution shows totally different changes compared with the 64-atom results.

As presented in the insets of Fig. 5(d), when the temperature quickly rises above the normal melting point, melting occurs when the superheated crystal generates a sufficiently large number of destabilized particles [29]. The appearance and growth of small liquid regions inside the crystal proceed from the melting process. From 35.00 to 37.80 ps, a solid and liquid phase coexist in the system, and well-defined crystal-liquid interfaces can be observed in a snapshot at 36.40 ps, identified by an extension of the common neighbor analysis method (ext-CNA) [26]. The behavior of the electronic structure thus exhibits hybrid characteristics of both phases as shown in Fig. 5(d). During the coalescence of the liquid regions, we can observe a gradual change of DOS from a solidlike semimetal phase to a liquidlike metal phase within $\sim$2.8 ps, different from the abrupt change in the 64-atom system results. We note that these results can hardly be achieved by the traditional *ab initio* method, and the DeepDOS model provides an opportunity to study the electronic structure for nonequilibrium processes, where both long-time ion dynamics and large system sizes are needed.

VI. CHARACTERIZING THE ATOMIC CONTRIBUTION TO TOTAL DOS

Based on the parametrized high-dimensional mapping between the local environment and atomic contribution to the total DOS, here we further investigate the temporal evolution of ADOS during the melting process. By applying a principal
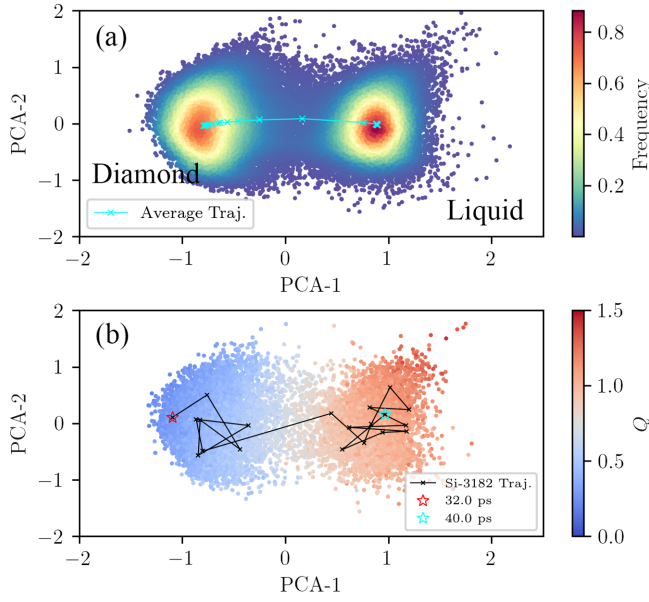
FIG. 6. (a), (b) PCA scatter plot of 81 920 ADOS from 20 snapshots of a 4096-atom system during the melting process, where the marker color indicates the frequency and ADOS-derived order parameter Q, respectively. The cyan line in (a) indicates the trajectories of averaged ADOS in PCA space during the melting process. In (b), a trajectory of Si-3182 atoms in ADOS-PCA space is highlighted with a black line.

component analysis (PCA), 81 920 ADOS extracted from 20 snapshots of a 4096-atom system during melting processes (from 34.0 to 40.0 ps) are projected onto two-dimensional principal component space.

As shown in Fig. 6(a), due to different characteristics in the ADOS curves, the distributions of ADOS are separated into two clusters corresponding to the diamond phase and liquid phase, while the transitional region between two phases represents the intermediate local structure such as strongly distorted crystalline generated during melting processes. The electronic feature of these intermediate structures exhibits a combination of liquid and solid phases, as reported in the previous section.

Choosing three electronic states from the local minimum in DOS at the Fermi level E_F, $\epsilon_1 \sim E_F - 8$ eV, and $\epsilon_2 \sim E_F - 5$ eV, a characteristic parameter $Q = g(E_F) + g(\epsilon_1) + g(\epsilon_2)$ for ADOS curves is given to describe the degree of disordered local environment for a selected atom. As presented in Fig. 6(b), the characteristic parameter gradually increases from $Q_{\min} \sim 0.19$ to $Q_{\max} \sim 1.46$ as the representative point in PCA subspace flows from a diamond region into a liquid region, indicating that such an ADOS-derived quantity can serve as a robust order parameter to identify the liquid phase, diamond phase, and intermediate structure.

The temporal evolution of ADOS during the melting process is presented in Fig. 7(b). Before the onset of melting at 32.0 ps, the representative points in PCA subspace concentrate to form the diamond-phase island. As melting occurs, with the coalescence of the liquid region and the movement of the liquid-solid interface, these representative points gradually flow away from the diamond region, and finally settle down in
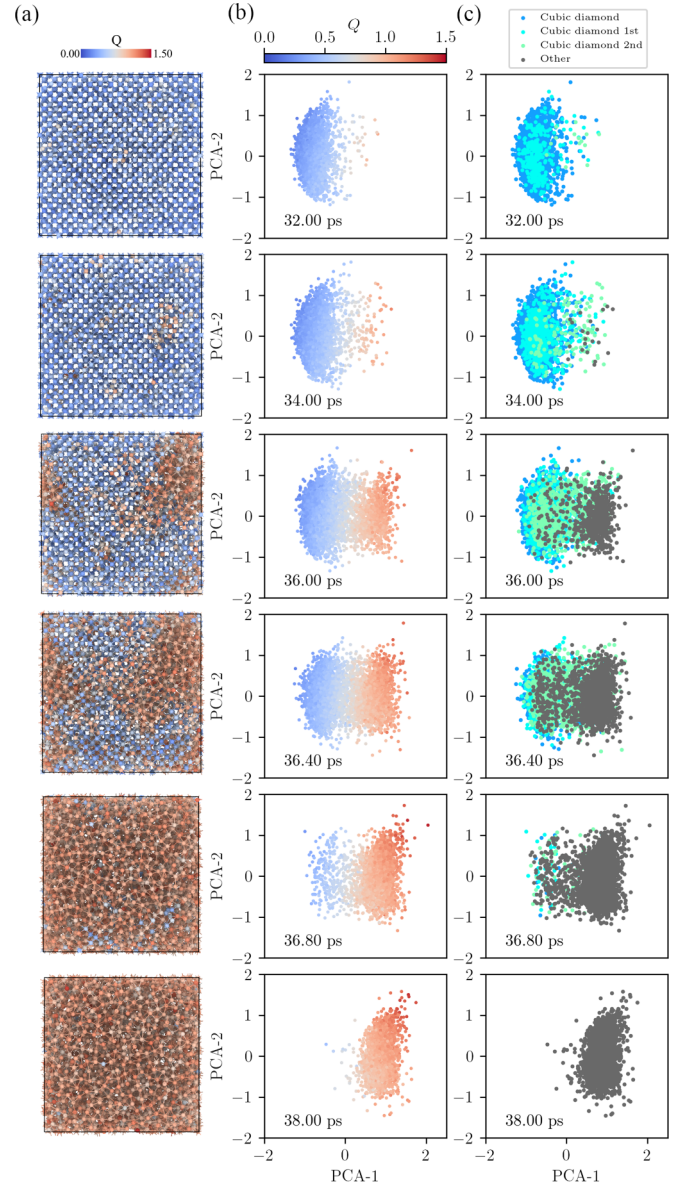

FIG. 7. (a) Snapshots of atomic configurations, colored by Q. (b), (c) Temporal evolution of ADOS in PCA subspace colored by the ADOS-derived order parameter Q and ext-CNA method, respectively.

the liquid-phase region, showing good consistency with the snapshots of atomic configurations in Fig. 7(a). We note that a significant amount of representative points are located in the transitional zone from 34.0 to 36.8 ps, with the characteristic parameter Q ranging from ~ 0.6 to ~ 0.8, indicating that the DNN-predicted ADOS and ADOS-derived order parameter Q accurately resolves the complex local environment for this nonequilibrium system that contains diamond crystalline, liquid, and thermally distorted intermediate structures.

For comparison, a traditional structure-identification method such as the ext-CNA method is used to classify the local structure. Based on the geometric feature of the atomic local neighborhoods for selected atoms, the ext-CNA method is sensitive to the structural noise driven by ionic thermal motion and phase transition dynamics, thus failing to classify

all these local structures correctly. As presented in Fig. 7(c), the distributions of predefined reference structures in the PCA subspace all overlap one another. These results indicate that the local electronic characteristics can achieve more accurate and robust performances in identifying different phases compared with geometrical characteristics such as the coordination number and bond-orientational order parameter.

VII. SUMMARY

For transient states that widely exist during dynamic processes, both the electronic structure and the atomic local neighborhoods can be strongly complicated by extreme thermodynamic conditions, inhomogeneity of the density distribution, and the coexistence and interface of different phases. Here, we demonstrate that our developed DeepDOS approach can not only serve as an efficient tool to study the temporal-spatial evolution of DOS during dynamic processes within the accuracy of the *ab initio* method, but also provide a possibility to distinguish different phases and identify hidden patterns through local electronic features.

Specifically, the accuracy and robustness of the Deep-DOS model are validated by reproducing DOS curves and band gaps for unseen atomic configurations generated by thermal fluctuation and density variations. Trained with a small-system data set, this size extensive model is able to give DOS curves for a large system. Therefore, a time-resolved diagnosis of DOS under isobaric heating conditions can be efficiently achieved by this machine-learning method, and we present the temporal evolution of DOS curves during melting processes that proceed by the nucleation and growth of the liquid region out of the solid matrix. Moreover, the electronic feature for local structures can also be accurately captured. As compared with geometric characteristics such as the ext-CNA method, the ADOS can give a relatively robust identification for local structures that significantly deviates from ideal crystal symmetry due to thermal fluctuation and phase transition dynamics.

In conclusion, this DeepDOS model can strongly enhance the further study of both electronic structures and ion dynamics during nonequilibrium processes created by ultrafast laser heating, shock loading, or a quasi-isentropic ramped pressure drive.

[1] Q. Zeng and J. Dai, Sci. China Phys., Mech. Astron. **63**, 263011 (2020).

[2] B. Chen, Q. Zeng, H. Wang, D. Kang, J. Dai, and A. Ng, arXiv:2006.13136.

[3] F. Soubiran and B. Militzer, Nat. Commun. **9**, 3883 (2018).

[4] B. Boates and S. A. Bonev, Phys. Rev. Lett. **110**, 135504 (2013).

[5] V. L. Deringer, N. Bernstein, G. Csányi, C. Ben Mahmoud, M. Ceriotti, M. Wilson, D. A. Drabold, and S. R. Elliott, Nature (London) **589**, 59 (2021).

[6] N. Jourdain, L. Lecherbourg, V. Recoules, P. Renaudin, and F. Dorchies, Phys. Rev. Lett. **126**, 065001 (2021).

[7] J. Behler and M. Parrinello, Phys. Rev. Lett. **98**, 146401 (2007).

[8] L. Zhang, J. Han, H. Wang, R. Car, and Weinan E, Phys. Rev. Lett. **120**, 143001 (2018).

[9] A. Chandrasekaran, D. Kamal, R. Batra, C. Kim, L. Chen, and R. Ramprasad, npj Comput. Mater. **5**, 22 (2019).

[10] C. Ben Mahmoud, A. Anelli, G. Csányi, and M. Ceriotti, Phys. Rev. B **102**, 235130 (2020).

[11] B. G. Del Rio, C. Kuenneth, H. D. Tran, and R. Ramprasad, J. Phys. Chem. A **124**, 9496 (2020).

[12] J. A. Ellis, L. Fiedler, G. A. Popoola, N. A. Modine, J. A. Stephens, A. P. Thompson, A. Cangi, and S. Rajamanickam, Phys. Rev. B **104**, 035120 (2021).

[13] Z. Lin, L. V. Zhigilei, and V. Celli, Phys. Rev. B **77**, 075133 (2008).

[14] B. Holst, V. Recoules, S. Mazevet, M. Torrent, A. Ng, Z. Chen, S. E. Kirkwood, V. Sametoglu, M. Reid, and Y. Y. Tsui, Phys. Rev. B **90**, 035121 (2014).

[15] S. Ono and T. Suemoto, Phys. Rev. B **102**, 024308 (2020).

[16] N. Jourdain, V. Recoules, L. Lecherbourg, P. Renaudin, and F. Dorchies, Phys. Rev. B **101**, 125127 (2020).

[17] L. Zhang, J. Han, H. Wang, W. Saidi, R. Car, and E. Weinan, in *Advances in Neural Information Processing Systems*, edited by S. Bengio, H. Wallach, H. Larochelle, K. Grauman, N. Cesa-Bianchi, and R. Garnett (Curran Associates, Inc., 2018), Vol. 31, pp. 4441–4451.

[18] H. Wang, L. Zhang, J. Han, and E. Weinan, Comput. Phys. Commun. **228**, 178 (2018).

[19] See Supplemental Material at http://link.aps.org/supplemental/10.1103/PhysRevB.105.174109 for details about the comparison of different loss functions, DP training, and thermally fluctuating DOS of the MgO system.

[20] S. Plimpton, J. Comput. Phys. **117**, 1 (1995).

[21] L. Zhang, D.-Y. Lin, H. Wang, R. Car, and Weinan E, Phys. Rev. Materials **3**, 023804 (2019).

[22] P. Giannozzi, O. Andreussi, T. Brumme, O. Bunau, M. B. Nardelli, M. Calandra, R. Car, C. Cavazzoni, D. Ceresoli, M. Cococcioni *et al.*, J. Phys.: Condens. Matter **29**, 465901 (2017).

[23] J. P. Perdew, K. Burke, and M. Ernzerhof, Phys. Rev. Lett. **77**, 3865 (1996).

[24] P. E. Blöchl, Phys. Rev. B **50**, 17953 (1994).

[25] N. Holzwarth, A. Tackett, and G. Matthews, Comput. Phys. Commun. **135**, 329 (2001).

[26] E. Maras, O. Trushin, A. Stukowski, T. Ala-Nissila, and H. Jonsson, Comput. Phys. Commun. **205**, 13 (2016).

[27] K. Lu and Y. Li, Phys. Rev. Lett. **80**, 4474 (1998).

[28] B. Rethfeld, K. Sokolowski-Tinten, D. von der Linde, and S. I. Anisimov, Phys. Rev. B **65**, 092103 (2002).

[29] Z. H. Jin, P. Gumbsch, K. Lu, and E. Ma, Phys. Rev. Lett. **87**, 055703 (2001).